




Modal analysis of actively controlled flow past a backward facing ramp

Matteo Chiatto * and Luigi de Luca 

*Department of Industrial Engineering, Aerospace Sector, Università degli Studi di Napoli “Federico II,”
Naples 80125, Italy*

Francesco Grasso 

DynFluid Laboratory, CNAM-Arts et Métiers, Paris 75003, France



(Received 26 February 2021; accepted 9 June 2021; published 28 June 2021)

An investigation based on the application of spectral proper orthogonal decomposition (SPOD) of pressure measurements and Fourier analysis of velocity measurements is carried out to further elucidate the properties of separated flow behind a backward-facing ramp in uncontrolled and controlled conditions. Several flow control conditions are considered, varying the duty cycle and the frequency of an actuation system composed of 89 pulsed jets, issuing normally to the flow direction. The SPOD is applied to unsteady pressure measurements to characterize the main features of the flow and to extract the most energetically and dynamically relevant space-time coherent structures. Fourier analysis is applied to the velocity measurements and is complementary to the SPOD analysis. In uncontrolled conditions four major modes, together with their typical frequencies, have been identified and associated with (1) presence of large-scale longitudinal roll-up vortices which oscillate at the slanted ramp side edges, (2) flapping motion of the central recirculation region, (3) large-scale vortex emission from the shear layer at the slant edge, and (4) onset of high-frequency Kelvin-Helmholtz instability occurring in the shear layer near the slant edge. The control suppresses the recirculation mode and all associated mechanisms. As expected, the mode related to the lateral roll-up vortices persists. The modal analysis also shows that distinctive peaked bands emerge, which are ascribed to the presence of the control pulsed jets. Focusing on the SPOD mode associated with the actuation allows one to analyze the extension of the receptivity region of the flow to the action of control. Some peculiar aspects of SPOD field reconstruction are suggested by the specific physical characteristics of the flow.

DOI: [10.1103/PhysRevFluids.6.064608](https://doi.org/10.1103/PhysRevFluids.6.064608)

I. INTRODUCTION

Flows around backward-facing ramps are representative of more complex flows of industrial interest occurring frequently around an automotive vehicle or an aerodynamic control surface. These flows generally exhibit a wide spectrum of spatial and temporal scales resulting from the underlying coherent structures characterizing the flow topology, which typically shows extended separation and shedding phenomena. Recognizing the features of coherent structures is an important aspect for the analysis of both numerical and experimental data to reduce the complexity of the governing equations and to formulate a reduced order model [1–3].

The flow over a backward-facing ramp exhibits an extended recirculation bubble having a two-dimensional character and the formation of two counter-rotating longitudinal vortices

*matteo.chiatto@unina.it

associated with three-dimensional effects due to the finite spanwise extent of the ramp [4–6]. Previous investigations, which focused on the analysis in the midlongitudinal plane, have also shown that the flow exhibits a dynamics related, on one hand, to the flapping motion of the separated flow and, on the other, to the formation of large-scale vortices along the separated shear layer and to turbulent motions [7].

The backward-facing ramp can model the rear part of an automobile [8], therefore this geometry has been widely studied to understand the base mechanisms of drag generation behind a vehicle. The timescales of the main coherent structures of the flow have been characterized numerically by Krajnovic and Davidson [9,10], analyzing both instantaneous and mean flow fields. The effect of the slant angle on the flow topology was experimentally investigated by Gillieron *et al.* [5] on the basis of pressure measurements and skin friction visualizations.

Due to the simplicity of its geometry, the backward-facing ramp has been one of the most studied cases to test the effectiveness of a control strategy. One of the first works dealing with the flow control over a slanted surface was presented by Brunn and Nitsche [11], exciting the shear layer with periodic perturbations. The most effective frequency, for flow control purposes, was found equal to that of the vortex-shedding process. Dandois *et al.* [12] numerically investigated the flow over a smooth ramp to test a synthetic jet device in reducing the separation length. They showed that forcing the flow at the natural shedding frequency produces a reduction of the separated zone, with the presence of a single large vortex and larger turbulent kinetic energy levels. Pamart *et al.* [13] emphasized the importance of choosing the optimal frequency and amplitude for each flow conditions. The same problem was addressed by Kumar and Alvi [14] using microjets as flow control devices. They concluded that the devices should be placed as close as possible to the separation line, the location and the injection angle of the actuators being key parameters for the control mechanism.

A further experimental characterization was presented by Debien *et al.* [15], who confirmed that an actuation frequency close to that of the vortex shedding produces a better reduction of separation length due to a lock-on effect; the same research group studied also the effect of a trailing edge flap in controlling the longitudinal pressure gradient, reporting a POD analysis on the velocity measurements [16]. A closed-loop control via a model-free genetic programming was applied by Debien *et al.* [17] to reduce the separated turbulent boundary layer over a sharp edge ramp using the signal of two hot-film sensors placed near the inflection point of the ramp and static pressure sensors along the ramp. Recently, Hlevca *et al.* [18] carried out a parametric study of the flow control with periodic pulsed jets actuators, by considering various combinations of frequencies and duty cycles, and keeping constant the blowing time.

The current study considers the same geometry analyzed by Hlevca *et al.* [18] and Chiatto *et al.* [19], focusing on the experimental characterization of the flow field in the rear region both in the absence of flow control and in controlled conditions. The investigation relies on unsteady surface pressure and hot-wire and stereo-PIV velocity measurements at various Reynolds numbers. The flow topology is reconstructed using the mean flow of the stereo-PIV measurements; the spatial and time evolution of coherent structures is characterized by spectral proper orthogonal decomposition (SPOD) [3]. Through the decomposition of the flow in the various SPOD pressure modes and Fourier analysis of the velocity, some further insight is gained into the physical mechanisms typical of the class of separated flows here analyzed. Moreover, the reattachment of the flow and thus the suppression of the recirculating bubble is highlighted by means of the SPOD, which represents a valuable tool to investigate the effectiveness of the applied control strategy and to evaluate the flow receptivity to the action of pulsed jets.

II. EXPERIMENTAL SETUP

The experimental configuration [18] consists of a backward-facing ramp of finite span slant angle $\alpha = 25^\circ$, streamwise length $L = 1.050$ m, spanwise extent $W = 0.389$ m, and height $H = 0.094$ m.

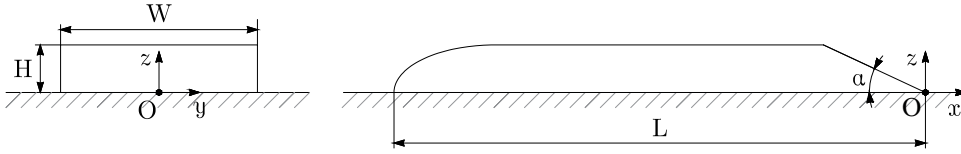


FIG. 1. Rear (left) and side (right) views of the model, with its geometrical parameters.

The geometric details of the ramp and the reference frame are given in Fig. 1 (note that the origin is located in the midlongitudinal plane at the end of the slant).

The analysis exploits the experimental database obtained in the S4 wind tunnel (a closed loop facility, equipped with a double duct air system with the test section in between) of the Institut Aérotechnique–Conservatoire National des Arts et Métiers, Paris.

The control system consists of an electromagnetic valve system to generate 89 pulsed jets with an operating frequency (f_a) and duty cycle (DC) ranging, respectively, from 50 to 250 Hz and from 25% to 60%. The round ended slots, as shown in Fig. 2 (left panel), are placed at a distance of $l = 10$ mm from the sharp edge, generating pulsed jets normal to the mean flow direction. They have a width of $w = 3$ mm and a height of $h = 1$ mm; their spacing is equal to $d = 4$ mm, with a curvature radius equal to $R = 0.5$ mm (Fig. 2, right panel).

The database includes pressure and velocity measurements at three free-stream velocities $U_\infty = 20, 30,$ and 40 m/s, corresponding to Reynolds numbers (based on the slant height) $Re_H = 1.4, 2.1,$ and 2.8×10^5 , respectively. Measurements were taken in both uncontrolled and controlled conditions, varying the frequency and the duty cycle of the pulsed jets. The control strategy relies on the injection of periodic perturbations before separation at the edge of the slant, keeping constant the blowing time at every Reynolds number, so as to excite the flow with the same jet structure over different actuation cycle extents. The operating characteristics of the test cases in controlled conditions are reported in Table I, which contains the Strohual number values ($St_a = f_a H / U_\infty$), as well as the actuation frequency f_a (expressed in Hz and given within the brackets), for the different Reynolds numbers and duty cycles.

As will be shown in Sec. IV, in the current work the analysis is carried out at the controlled conditions corresponding to the optimal conditions for drag reduction.

In more detail, we have analyzed the following:

(1) Stereo-PIV velocity measurements (2D-3C) at four longitudinal (x - z) and eight (y - z) planes of 400 mm \times 400 mm; the laser light is provided by a 200 mJ Nd:Yag laser (Dantec), acquiring the images with two FlowSense EO 4 megapixels CCD cameras at a frequency of 8 Hz (780 snapshots for each measuring plane). The velocity fields are computed with a multipass algorithm with a final size of the interrogation windows equal to 32×32 pixels (50% overlapped) [18]. The PIV measuring planes are shown in Fig. 3.

(2) Unsteady pressure measurements using 62 Kulite miniature pressure sensors (type XCQ-093-1D) flush-mounted on the slant surface (55 on half of the slant and 7 in the longitudinal midplane downstream of the slant hinge line). The pressure is acquired at a sampling frequency of 20 kHz. To enhance the spatial resolution of the pressure measurements within the recirculation

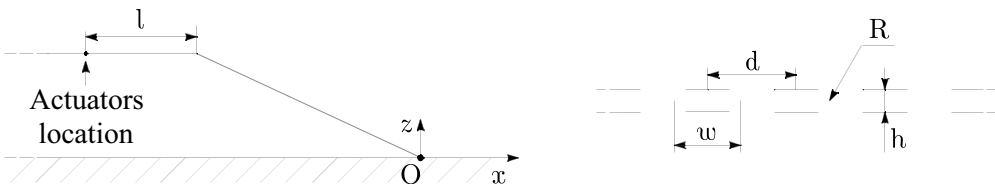


FIG. 2. Location (left) and geometrical characteristics (right) of the actuators.

TABLE I. Experiments test matrix: Strohal number values and corresponding actuation frequencies in Hz (in brackets) for different Reynolds numbers and duty cycles.

Re_H	Duty cycle (%)			
	25	40	50	60
1.4×10^5	0.45 (95)	0.71 (152)	0.89 (190)	1.07 (228)
2.1×10^5	0.28 (90)	0.45 (144)	0.56 (180)	0.68 (216)
2.8×10^5	0.20 (85)	0.32 (136)	0.40 (170)	0.48 (204)

zone and to better characterize the flow field at the ramp sides, the probes were clustered along the centerline and at the ramp edges. Twenty pressure probes were placed in the streamwise direction along the centerline, with a spacing $\Delta x/H \approx 0.14$, $\Delta x/H \approx 0.18$ at the ramp spanwise ends, and $\Delta x/H \approx 0.56$ in the middle zone. The probes were distributed in the spanwise direction with a spacing $\Delta y/H \approx 0.2$. The position of the Kulite sensors is shown in Fig. 4 (left panel).

(3) Two-component hot-wire measurements (Dantec 55P61 hot-wire miniature probe in conjunction with a Dantec StreamLine unit, with the same sampling frequency as the Kulite sensors) acquired in two longitudinal planes (at the midplane $y/H = 0$ and at $y/H = 1.9$), each of them containing nine probes located in the shear layer and in the core of the recirculation bubble (Fig. 4, right panel). The location of the hot-wire probes is reported in Table II.

III. METHODOLOGY

In this section we briefly present the SPOD and the two-point cross-correlation analysis that have been applied to the unsteady pressure measurements to characterize the features of the flow over the slant.

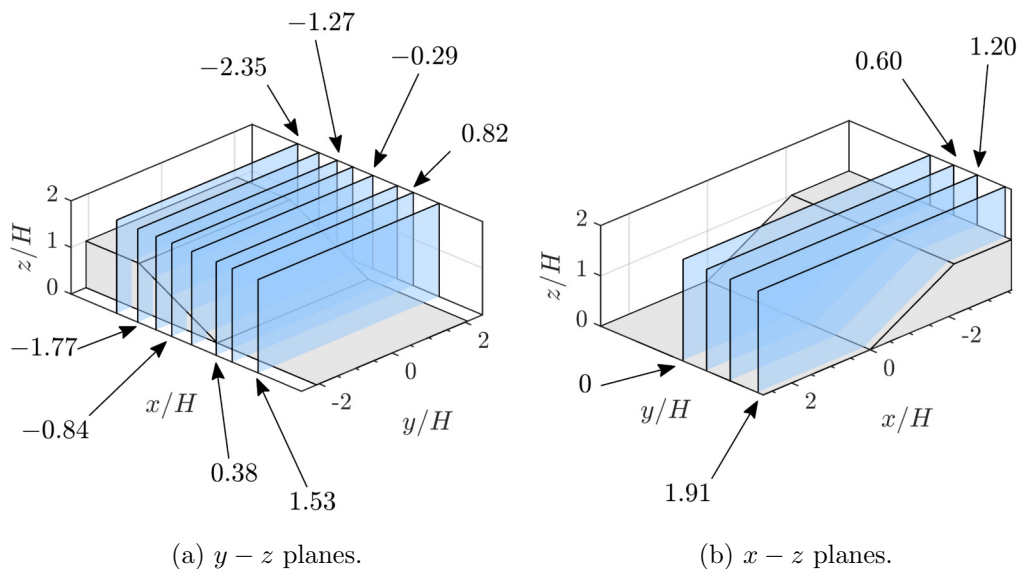


FIG. 3. Location of PIV measurement planes. The arrows indicate the positions in terms of x/H (a) and y/H (b).

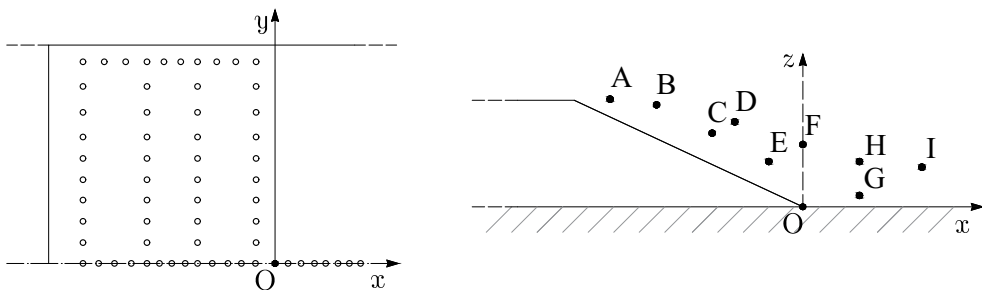


FIG. 4. Location of Kulite pressure probes (left), and hot-wire probes (right).

A. SPOD analysis

Following Ref. [3], given a stochastic field $\mathbf{q}(\mathbf{x}, t)$ at discrete times (each time t corresponds to a snapshot of the flow field) and position \mathbf{x} , we define its fluctuation as

$$\mathbf{q}'(\mathbf{x}, t) = \mathbf{q}(\mathbf{x}, t) - \bar{\mathbf{q}}(\mathbf{x}), \quad (1)$$

where $\bar{\mathbf{q}} = E\{\mathbf{q}(\mathbf{x}, t)\}$ is the ensemble average (“time” average over all snapshots, with $E\{\cdot\}$ the expectation operator). Using SPOD one can then determine the representation in the space-time domain that best approximates $\mathbf{q}'(\mathbf{x}, t)$ with the least number of modes.

The SPOD modes that represent the eigenvectors of the cross-spectral density tensor \mathbf{S} are estimated via the Welch periodogram method [20]. Accordingly, an ensemble of realizations of the temporal Fourier transform of the data is constructed by subdividing the total number of snapshots in N_b blocks of equal length N_f (N_f being the number of snapshots per block): $\mathbf{Q}^{(j)} = [\mathbf{q}_1^{(j)}, \mathbf{q}_2^{(j)}, \dots, \mathbf{q}_{N_f}^{(j)}]$, with $j = 1, \dots, N_b$. Each block (or segment) overlaps the adjacent block (we have used 50% overlap). Note that the superscript $\{\cdot\}'$ (which stands for fluctuation) has been omitted.

For each segment, the weighted discrete Fourier transform in time, $\hat{\mathbf{Q}}^{(j)} = \mathcal{F}\{\mathbf{Q}^{(j)}\mathbf{W}_T\}$, is first computed, where \mathbf{W}_T is the diagonal matrix containing the window weights, generally equal for all Fourier realizations. Then the matrix containing all Fourier transform realizations at the k th frequency, $\hat{\mathbf{Q}}_k = [\hat{\mathbf{q}}_k^{(1)}, \hat{\mathbf{q}}_k^{(2)}, \dots, \hat{\mathbf{q}}_k^{(N_b)}]$, is obtained. The spectral cross-correlation tensor of the ensemble of the transformed data is calculated one frequency at a time, $\mathbf{S}_k = \hat{\mathbf{Q}}_k \hat{\mathbf{Q}}_k^*$, and the SPOD modes (Ψ_k) are determined.

Once the main SPOD modes have been computed, it is possible to reconstruct the fluctuations field coming back to the time domain. Nekkanti and Schmidt [21] have recently presented a Fourier-time analysis and a low-rank reconstruction of turbulent flows using SPOD. Following their approach, the data are reconstructed in the frequency domain as a combination of the corresponding SPOD modes. Thus, the Fourier realizations at the k th frequency can be written as $\hat{\mathbf{Q}}_k = \Psi_k \mathbf{A}_k$, where \mathbf{A}_k is the expansion coefficients matrix and a function of the specific frequency. Each Fourier

TABLE II. Locations of the analyzed hot-wire probes.

Ref.	A	B	C	D	E	F	G	H	I
x/H	-1.81	-1.28	-0.85	-0.64	-0.32	0	0.53	0.53	1.12
z/H	1.01	0.96	0.69	0.80	0.43	0.59	0.11	0.43	0.37

realization of the j th mode is expressed in the form

$$\hat{\mathbf{q}}_k^{(j)} \approx \sum_{l=1}^r \boldsymbol{\psi}_{k,l} a_{l,j}^k, \quad (2)$$

where l is the running index associated with the number of SPOD modes used to reconstruct the generic Fourier realizations of the j th mode (note that the equation is approximate only when $l = 1, \dots, r$, with r less than the number of nonzero eigenvalues of \mathbf{S}_k).

Once all $\hat{\mathbf{Q}}_k$ have been reconstructed, the Fourier realizations are rearranged into the block form $\hat{\mathbf{Q}}^{(j)} = [\hat{\mathbf{q}}_1^{(j)}, \hat{\mathbf{q}}_2^{(j)}, \dots, \hat{\mathbf{q}}_{N_r}^{(j)}]$, and, through the inverse weighted Fourier transform $\mathbf{Q}^{(j)} = \mathcal{F}^{-1}\{\hat{\mathbf{Q}}^{(j)} \mathbf{W}_T^{-1}\}$, the original snapshots are retrieved. The last step of the reconstruction procedure requires an appropriate choice of the overlapped snapshots. Indeed, a nonzero overlap introduces an ambiguity for all snapshots belonging to two different blocks. Nekkanti and Schmidt [21] proposed different approaches to remove this ambiguity, showing that the most successful one, in terms of 2-norm error, considers the snapshots with the higher windowing weight. The procedure has been implemented in MATLAB.

B. Two-point cross-correlation analysis

To further characterize the dynamics of the coherent structures, we have also evaluated the convective velocity, which represents the velocity at which structures shed at the slant edge are convected. In particular, the convection velocity in the longitudinal direction is evaluated from the space-time cross-correlation tensor of the pressure fluctuation, p' , as described below.

The normalized two-point space-time correlation tensor, $\mathbf{C}(x_0, \Delta x, y, t, \tau)$, is defined as

$$\mathbf{C}(x_0, \Delta x, y, t, \tau) = \frac{E\{p'(x_0, y, t) p'(x_0 + \Delta x, y, t + \tau)\}}{E\{p^2(x_0, y, t)\}^{1/2} E\{p^2(x_0 + \Delta x, y, t + \tau)\}^{1/2}}, \quad (3)$$

where x_0 is the reference location, and Δx and τ are, respectively, the separation distance and the time lag.

\mathbf{C} exhibits a peak when probes record similar pressure signals at different time instances and locations. The time at which this peak occurs represents the average time during which the structures move downstream (respectively, upstream) from $x = x_0$ to $x = x_0 + \Delta x$ (respectively, $x = x_0 - \Delta x$), and correspondingly the streamwise convection velocity (U_c) can be estimated [22].

IV. RESULTS AND DISCUSSION

This section reports the results for both uncontrolled and controlled conditions: first, the mean flow topology, reconstructed by interpolating the mean flow of the stereo-PIV measurements, is briefly discussed; second, a SPOD analysis is applied to the unsteady pressure and stereo-PIV velocity measurements; then a comparison with the hot-wire velocity measurements is also carried out; finally, further physical considerations, together with the pressure fields reconstruction, are presented.

Starting from the case at $\text{Re}_H = 1.4 \times 10^5$ in uncontrolled conditions, Fig. 5 shows the shape of the recirculating bubble in the $y/H = 0$ plane and its extension on the surface of the model, together with 3D streamlines and the vortical structures at the sides of the slant.

The (mean) flow separates at the beginning of the ramp and reattaches approximately at $\ell_r/H = 3$, where ℓ_r is the reattachment length, measured in the streamwise direction from the beginning of the slant to the reattachment point. The flow above the recirculation zone moves downstream, following its curvature. The bubble extension reduces in the spanwise direction. At the side of the ramp, the flow field is dominated by two counter-rotating structures, which affect the entire spanwise velocity distribution, producing not negligible three-dimensional effects, and increase their dimensions moving downstream. These structures have been visualized through the λ_2 method.

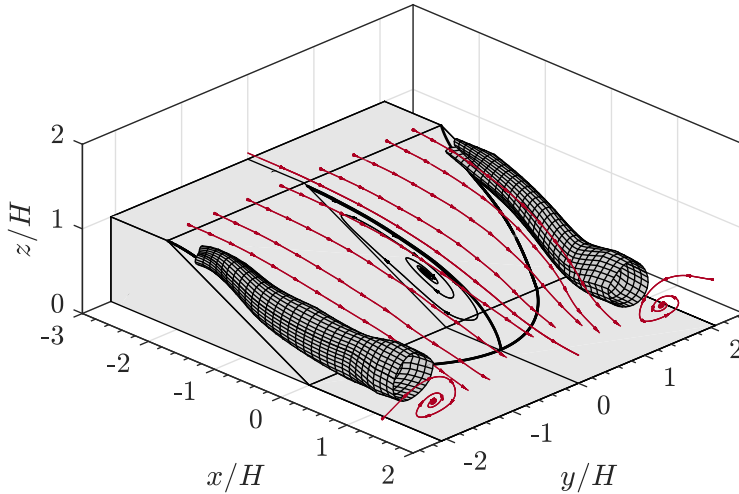


FIG. 5. Reconstruction of the flow topology from stereo-PIV measurements in uncontrolled conditions at $Re_H = 1.4 \times 10^5$.

Increasing the Reynolds number, the extension of the recirculating bubble is reduced, while the vortical structures persist at the ramp edges.

The effect of control is to suppress the recirculation bubble, promoting the reattachment of the flow. Figure 6 refers to the controlled case at $Re_H = 2.1 \times 10^5$ and $St_a = 0.56$. It is worth noting that the streamlines now follow the shape of the slant, except in the midplane where a weak one-sided vortical structure arises (starting from about half slant); the presence of this nonsymmetric vortex is attributed to the operation of the present actuation system. Moreover, the two counter-rotating vortices (visualized through the same λ_2 method) still dominate the flow at the sides of the ramp; they appear with a reduced extension and with an increased core distance with respect to the corresponding uncontrolled case.

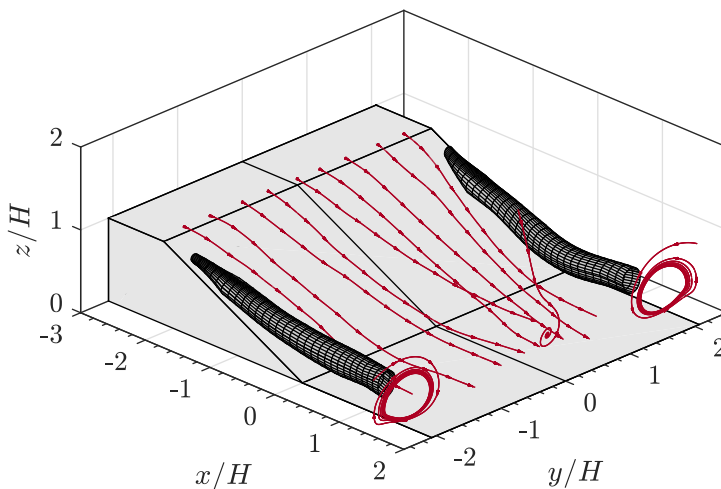


FIG. 6. Reconstruction of the flow topology from stereo-PIV measurements in controlled conditions ($St_a = 0.56$) at $Re_H = 2.1 \times 10^5$.

TABLE III. Pressure drag coefficients at various Reynolds numbers for all experimental cases.

Re_H	C_D				
	Uncontrolled flow	Controlled flow, DC (%)			
		25	40	50	60
1.4×10^5	0.2012	0.0652	0.0649	0.0641	0.0436
2.1×10^5	0.2214	0.0935	0.0920	0.0894	0.0940
2.8×10^5	0.2427	0.1483	0.1425	0.1322	0.1317

In previous work [18] the effectiveness of the control strategy was evaluated in terms of the pressure drag gain, where the drag was calculated from steady pressure measurements in the longitudinal midplane. In the present work the drag has been evaluated considering the unsteady pressure and velocity measurements over the entire slant surface [23].

The pressure coefficient at the i th pressure probe is defined as $C_{p,i} = 2(p_i - p_\infty)/\rho_\infty U_\infty^2$, where p_∞ and ρ_∞ are the static pressure and the density of the flow upstream of the model, respectively. Thus, the pressure drag coefficient (C_D) is evaluated as the projection (in the streamwise direction) of the pressure coefficients of the probes located on the slant surface:

$$C_D = -2 \frac{\sin(\alpha)}{HW} \sum C_{p,i} \Delta s_i, \quad (4)$$

where the factor 2 has been introduced to consider the whole slant surface. Δs_i represents the part of the slant surface, which has been adequately partitioned in the spanwise and streamwise directions, so that its centroid coincides with the i th pressure probe location. Table III reports the estimated pressure drag coefficients for all experimental cases at various Reynolds numbers and operating duty cycle values (for the corresponding actuation frequencies refer to Table I). Note that the minimum values, for each Reynolds number, are indicated in bold. As expected, the unsteady pressure measurements give slightly different values than the steady ones; nonetheless the resulting frequencies and duty cycles are unaffected and are given for convenience in Table IV.

A. Spectral POD analysis

The flow field dynamics is strongly influenced by the control strategy. To investigate the effects of the actuation on the main flow mechanisms, it is convenient to consider first the uncontrolled conditions and then to focus on the controlled cases (presented in detail only for optimal flow control conditions of Table IV).

Six million snapshots have been considered for the analysis, and the pressure data have been subdivided in 300 blocks ($N_b = 300$) of equal length ($N_f = 20\,000$). Spectral leakage is reduced with a standard Hamming window with 50% overlap. Figure 7 shows the eigenvalues of the first 10 modes as a function of the Strouhal number at the three Reynolds numbers (note that the eigenvalues have been normalized by total energy) for the uncontrolled conditions.

TABLE IV. Optimal flow control conditions.

Re_H	Optimal flow control conditions		
	DC (%)	St_a	f_a (Hz)
1.4×10^5	60	1.07	228
2.1×10^5	50	0.56	180
2.8×10^5	60	0.48	204

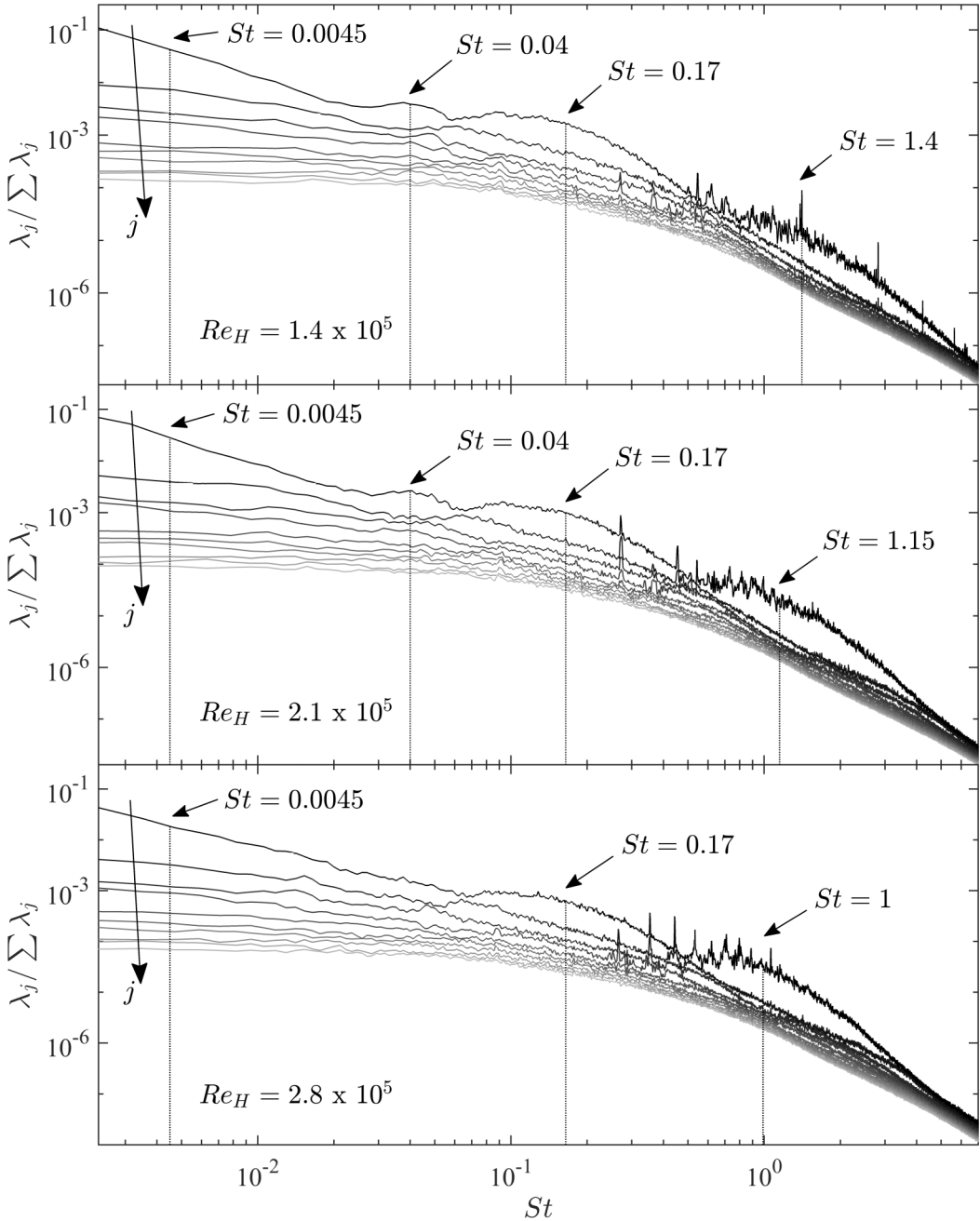


FIG. 7. Spectral eigenvalues as a function of the Strouhal number for $Re_H = 1.4$ (top panel), 2.1 (mid-panel), and 2.8×10^5 (bottom panel). Arrows, labeled j , indicate increasing order of modes, with j the running index associated with the modes.

The spectra have been filtered for Strouhal numbers higher than $St \geq 7$, characterized by a strong noise attributed to the electrical power supply (motor inverter) of the wind tunnel fans.

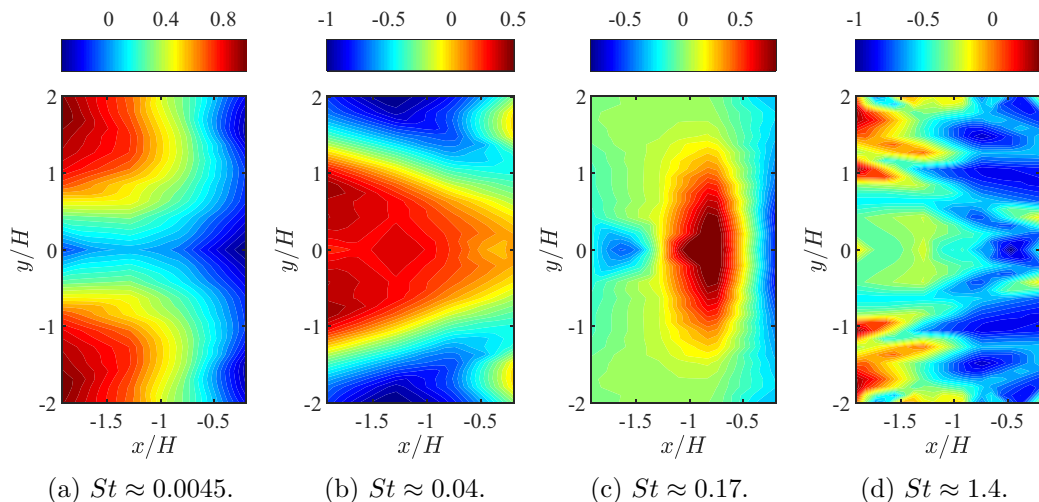


FIG. 8. Spatial structure of the main frequencies of the first SPOD pressure mode at $Re_H = 1.4 \times 10^5$. For each panel the flow direction is from left to right. The surface contours represent the normalized pressure fluctuation signature on the ramp.

The figure highlights that for the three Reynolds numbers in certain frequency ranges the spectra exhibit a clear separation between the first and the other modes, an indication that the flow has a low-rank behavior. This also suggests the occurrence of different controlling mechanisms that dominate in the various frequency bands, whose common characteristic is that the local peaks are not sharp, but they emerge from smooth bell-shaped trends. This feature has implications in the reduced order reconstruction of the field (this point will be discussed in Sec. IV D). Note that the arrows in the figure (except the first one, as will be clarified below) point to the maximum difference between the first and second SPOD modes.

The spatial structure corresponding to the dominant frequencies of the first SPOD mode is depicted in Fig. 8, which shows the surface contour of the pressure fluctuations on the slant at four Strouhal numbers and at $Re_H = 1.4 \times 10^5$. (Note that these Strouhal numbers correspond to the dominant frequencies of the velocity spectra, discussed in Sec. IV B.) The data have been interpolated on a finer grid and reported on a restricted ramp surface delimited by $-1.9 \leq x/H \leq -0.2$ and $-2 \leq y/H \leq 2$; the x coordinate is measured horizontally. The spatial distribution of these modes remains substantially unchanged with the Reynolds number.

For very low Strouhal numbers ($St < 10^{-2}$, corresponding to frequencies approximately less than 1 Hz), the figure shows a large separation between the first mode and the higher ones. The flow oscillation occurring at these low frequencies is due to the flow roll-up at the slant side edges leading to the formation of two counter-rotating longitudinal structures. The spatial structure of the pressure field is shown in Fig. 8(a) for $St = 0.0045$, which corresponds to the frequency detected by hot-wire measurements at probes B, G, and I in the plane $y/H = 1.9$. It is interesting to observe that, due to the presence of the two roll-up vortices, large pressure variations occur at the side edges of the model, while the pressure remains almost constant at the center of the ramp.

The dynamics of these vortical structures is also confirmed by the SPOD analysis (considering 30 blocks, each one composed of 60 snapshots, with a 50% overlap) of the stereo-PIV velocity measurements. In Fig. 9 we show the isocontour of the first SPOD mode associated with the spanwise (left panel) and crosswise (right panel) normalized velocity at $St \approx 0.0045$ in the plane $x/H = -1.27$ downstream of probe B. The figure reveals the occurrence of two vortices that exhibit

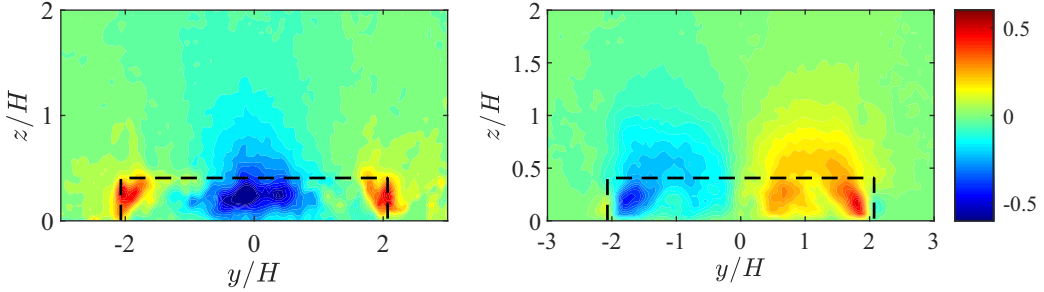


FIG. 9. Spatial structure of the main frequencies of the first SPOD velocity mode at $St = 0.0045$ and $Re_H = 1.4 \times 10^5$. The contours represent the normalized spanwise (left panel) and crosswise (right panel) velocity fluctuations in the $x/H = -1.27$ plane. The black dashed line is the slant projection in the measuring plane.

an in-phase clockwise motion in the transverse plane and corroborates the SPOD results shown in Fig. 8(a).

For higher Reynolds numbers, the topology of the flow at the slant side edges remains substantially unchanged. The spectra exhibit a larger separation between the first and the higher modes, and the corresponding SPOD structures (not reported) preserve the same spatial pattern.

In the band corresponding to $0.025 < St < 0.055$ and centered around $St \approx 0.04$, at $Re_H = 1.4 \times 10^5$ the flow exhibits a dominant frequency $f \approx 9$ Hz, which is associated with the flapping motion of the recirculation zone forming on the slant. Note that if one expresses the Strouhal number in terms of the reattachment length ℓ_r (which for $Re_H = 1.4 \times 10^5$ is $\ell_r/H \approx 3$) one finds $St_{\ell_r} \approx 0.12$, which is in very good agreement with values reported in similar studies [7,24]. The spatial structure of the first SPOD mode in this frequency range is reported in Fig. 8(b). It presents a uniform zone, associated with the flapping motion, which is concentrated in the center-upper part of the ramp and resembles the shape of the recirculating bubble.

At $Re_H = 2.1 \times 10^5$ the region of mode separation is still clearly visible, preserving a peak at $St \approx 0.04$. The reattachment point is displaced upstream moving closer to the hinge line ($\ell_r/H \approx 2.8$), limiting the pressure variations to a reduced portion (with respect the previous Re_H) of the ramp. This is also confirmed by the corresponding SPOD spatial distribution, shown in Fig. 10(a), which presents a uniform pressure signature in the upper central part of the slant; the reattachment Strouhal number St_{ℓ_r} remains unchanged. Further increasing the Reynolds number ($Re_H = 2.8 \times 10^5$), the extent of the recirculating bubble is reduced, and the energy associated with this spectral band decreases and the modes no longer exhibit a clear separation (Fig. 7). However, the corresponding SPOD structures still show a spatial distribution similar to that observed at lower Reynolds numbers, but with a further reduction in the uniform pressure zone extension [Fig. 10(b)].

The reduction of the recirculating bubble extension provides further information on the nature of the incoming boundary layer. The work by Armaly *et al.* [25], although it refers to a different geometry (backward-facing step) in a two-dimensional channel, can be considered as a reference work. Armaly *et al.* experimentally observed that the variation of the reattachment length depends on the flow regime and therefore changes with the Reynolds number. They showed that in the laminar regime the reattachment length increases nonlinearly with the Reynolds number. The transitional regime is characterized by a reattachment length that, after a sharp decrease, attains a minimum and then increases to a practically constant value, a feature of the turbulent flow regime. Based on these considerations, one can conclude that, for the present configuration, the flow is in the transitional regime.

A clear separation of modes is observed in the range $0.055 < St < 0.45$ peaked at $St \approx 0.17$, which corresponds for $Re_H = 1.4 \times 10^5$ to a frequency $f \approx 40$ Hz. This frequency is typical of the shedding mechanism of large-scale vortices from the separation bubble, and its value is in agreement with the experimental findings of Kiya and Sasaki [24] and Cherry *et al.* [26] and is related to

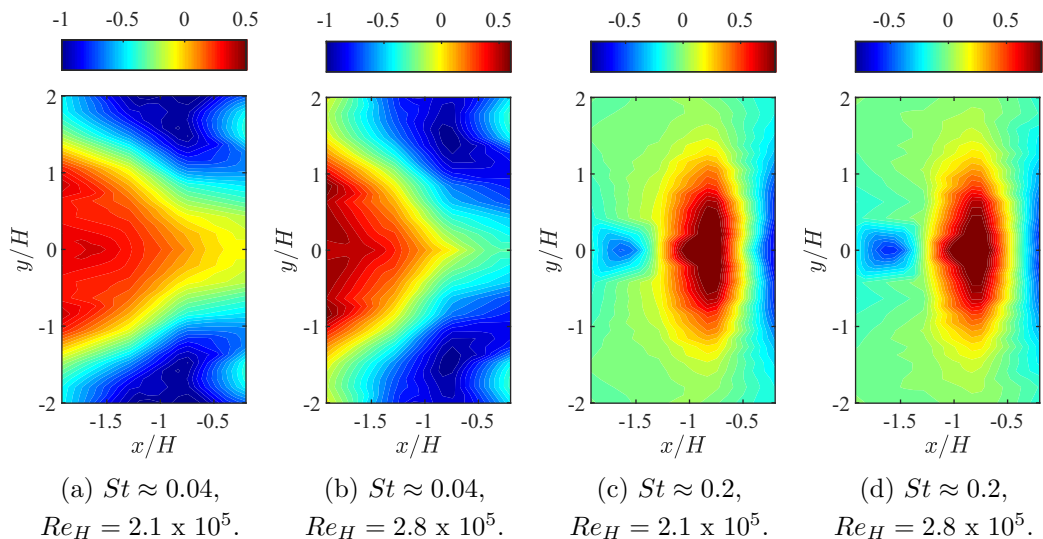


FIG. 10. Spatial structure of the main frequencies of the first SPOD pressure mode at $Re_H = 2.1$ and 2.8×10^5 . For each panel the flow direction is from left to right. The surface contours represent the normalized pressure fluctuation signature on the ramp.

the edge tone phenomenon [27], which will be discussed in Sec. IV C. The corresponding SPOD structure is shown in Fig. 8(c), that represents the pressure fluctuation due to the vortex transition, and its dimension slightly reduces as Re_H increases [Figs. 10(c) and 10(d)].

In the frequency band of $0.6 < St < 4$, the spectrum is much more noisy, with a peak at $St = 1.4$ ($f = 300$ Hz). As also observed in Ref. [7], these relatively high frequencies are ascribed to the onset of Kelvin-Helmholtz instability occurring in the thin shear layer near the slant edge. The corresponding spatial structure of this mode is rather complex, exhibiting localized pressure fluctuations on the slant [Fig. 8(d)], and a streaky pressure pattern converging towards the symmetry axis. At higher Reynolds numbers, the spectra exhibit a slight reduction in the peak value, but the main features of this frequency range are substantially unaffected (not reported for brevity).

The values of the Strouhal number associated with the most energetic and dynamically relevant coherent structures have been summarized in Table V at various Reynolds numbers.

In controlled conditions the spectra obtained for the three Reynolds numbers are shown in Fig. 11. Comparing the controlled spectra with the uncontrolled ones, several differences can be noted. For $St < 0.5$, the distribution of power per mode exhibits a more uniform distribution than in uncontrolled conditions due to the removal of flapping and vortex emission from the shear layer.

For $St < 10^{-2}$ at $Re_H = 1.4 \times 10^5$ a large separation between the first and the higher modes, due to the formation of the two counter-rotating longitudinal structures at the slant side edges,

TABLE V. Strouhal number values associated with the most energetic and dynamically relevant coherent structures at different Reynolds numbers in case of uncontrolled conditions.

	$Re_H = 1.4 \times 10^5$	$Re_H = 2.1 \times 10^5$	$Re_H = 2.8 \times 10^5$
St_1	≈ 0.0045	≈ 0.0045	≈ 0.0045
St_2	≈ 0.04	≈ 0.04	Not detected
St_3	≈ 0.17	≈ 0.17	≈ 0.17
St_4	≈ 1.4	≈ 1.15	≈ 1

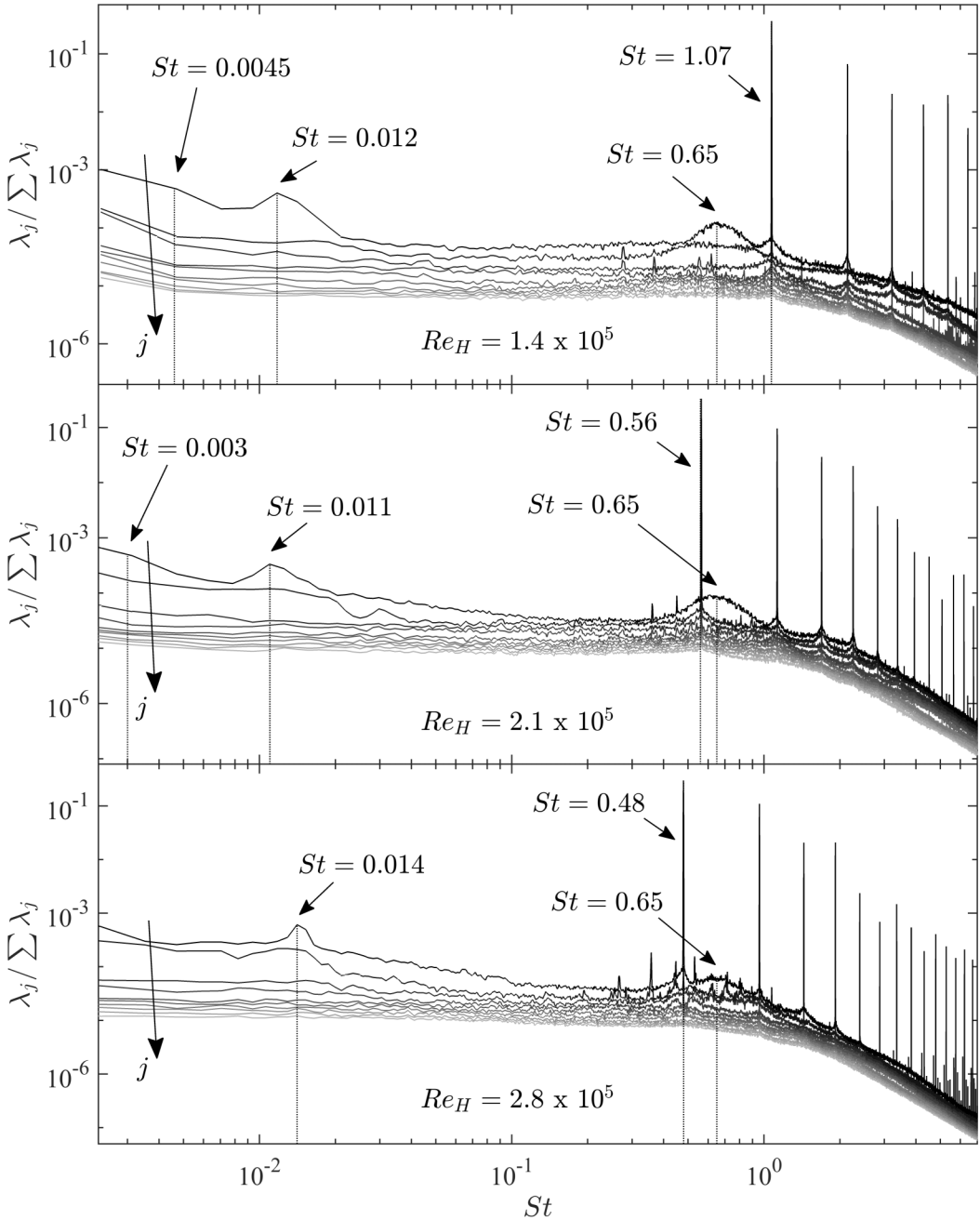


FIG. 11. Spectral eigenvalues as a function of the Strouhal number for $Re_H = 1.4$ (top panel), 2.1 (mid-panel), and 2.8×10^5 (bottom panel) in optimal controlled conditions. Arrows, labeled j , indicate increasing order of modes, with j the running index associated with the modes.

is observed. Due to the action of the control the longitudinal vortices strengthen, their core size reduces and the core distance increases. The corresponding pressure variations on the slant surface [Fig. 12(a)] are mainly concentrated at the side edges of the ramp.

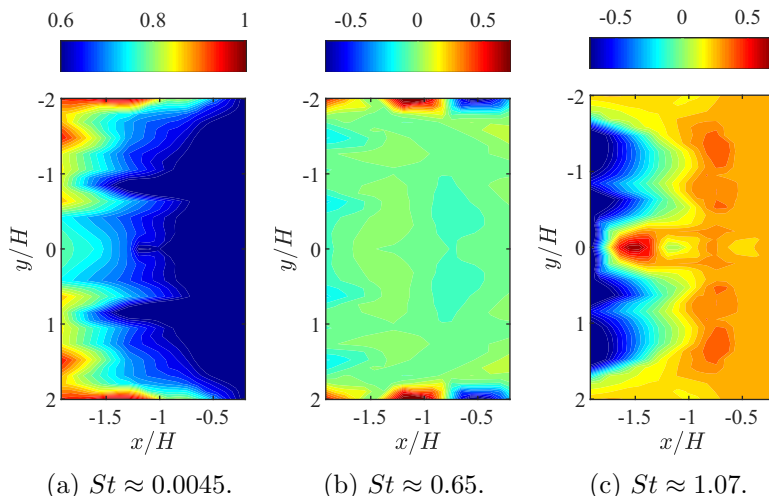


FIG. 12. Spatial structure of the main frequencies of the first SPOD pressure mode at $Re_H = 1.4 \times 10^5$ ($St_u = 056$). For each panel the flow direction is from left to right. The surface contours represent the normalized pressure fluctuation signature on the ramp.

The dimensions of these vortical structures decrease with increasing the Reynolds number, leading to a more uniform spectrum. The present spectral interval appears quite reduced at $Re_H = 2.1 \times 10^5$ and then disappears at $Re_H = 2.8 \times 10^5$.

In the range $0.009 < St < 0.019$ the lowest Re_H case exhibits a second bump centered around $St \approx 0.012$, which corresponds to the presence of the one-sided streamwise vortex structure around the midplane, already observed in Fig. 6 and reported in [18]. The pressure signature associated with this frequency band [Fig. 13(a)] is nonsymmetric, with a maximum (red area) localized near the hinge line at $y/H \approx 0.5$.

Increasing the Reynolds number, the peak exhibits a slight variation going from $St \approx 0.011$ at $Re_H = 2.1 \times 10^5$ to $St \approx 0.014$ at 2.8×10^5 , respectively, with a spectral extension gradually smaller. The corresponding SPOD structures [Figs. 13(b) and 13(c)] show that the high-pressure

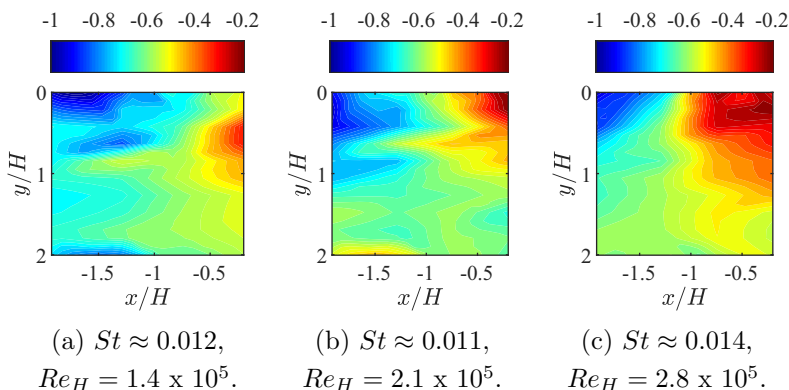


FIG. 13. Spatial structure of the main frequencies of the first SPOD pressure modes at $Re_H = 2.1$ and 2.8×10^5 . For each panel the flow direction is from left to right. The surface contours represent the normalized pressure fluctuation signature on a one-sided half ramp.

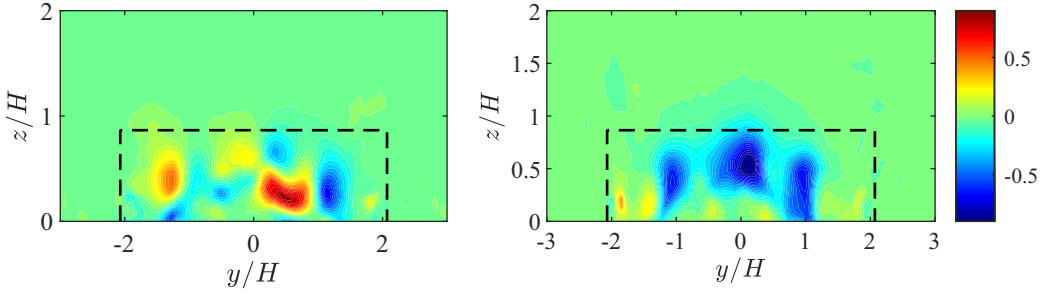


FIG. 14. Spatial structure of the main frequencies of the first SPOD velocity mode at $St = 0.011$ and $Re_H = 2.1 \times 10^5$. The contours represent the normalized spanwise (left panel) and crosswise (right panel) velocity fluctuations in the $x/H = -1.27$ plane. The black dashed line is the slant projection in the measuring plane.

values move upstream towards the midplane, and the formation of the vortex structure occurs early in the longitudinal direction. To shed further light on this occurrence, the SPOD technique (considering 30 blocks, each one composed of 60 snapshots, with a 50% overlap) has been applied to the stereo-PIV velocity measurements. Figure 14 depicts the spatial distributions of the normalized spanwise (left panel) and crosswise (right panel) velocity fluctuations associated with $St \approx 0.011$ at $Re_H = 2.1 \times 10^5$ in the $x/H = -0.29$ plane. These distributions confirm the nonsymmetric nature of the mode, whose main structure is located, both in the SPOD pressure distribution [Fig. 13(b)] and in the velocity data (Fig. 14, left panel), between $0 \leq y/h \leq 1$.

Another interval of interest for the $Re_H = 1.4 \times 10^5$ case extends between $0.48 < St < 0.88$, with a peak at $St \approx 0.65$. For the uncontrolled case these frequencies have been ascribed to the onset of Kelvin-Helmholtz instability occurring in the thin shear layer near the sharp edge. The actuation system removes this mechanism on the whole ramp except near the slant edges because, for manufacturing reasons, the pulsed jets are not active in these regions. Indeed, the structures associated with this spectral band exhibit pressure fluctuations localized at the slant edges only [Fig. 12(b)], and the same behavior is observed for the other two Reynolds numbers (not reported).

Finally, the last significant frequency band is characterized by the peak associated with the action of the control. It corresponds to the actuation frequency of the pulsed jets. This is the eigenvalue highest value and affects the whole spectrum with its higher harmonics; actuation inhibits vortex pairing and no subharmonics are detected. The corresponding pressure distribution on the slant presents a low-pressure area close to the slant edge with a slight spanwise modulation, due to the momentum injection of the pulsed jets, followed by a pressure recovery region (again spanwise modulated). Depending on the flow regime and the control conditions, the recovery region can extend to the whole slant surface, as for the $Re_H = 1.4 \times 10^5$ case shown in Fig. 12(c), or it can be characterized by more complex patterns, as will be shown hereafter.

For clarity, the characteristic Strouhal number values for controlled conditions, associated with the most energetic and dynamically relevant coherent structures, are summarized in Table VI for

TABLE VI. Strouhal number values associated with the most energetic and dynamically relevant coherent structures at different Re numbers in case of controlled conditions.

	$Re_H = 1.4 \times 10^5$	$Re_H = 2.1 \times 10^5$	$Re_H = 2.8 \times 10^5$
St_1	≈ 0.0045	≈ 0.003	Not detected
St_2	≈ 0.012	≈ 0.011	≈ 0.014
St_3	≈ 0.65	≈ 0.65	≈ 0.65
St_4	$= 1.07$	$= 0.56$	$= 0.48$

all Reynolds numbers; the table should be compared with the one corresponding to uncontrolled conditions (Table V).

Although the actuation removes the recirculation bubble in all configurations, the resulting pressure distribution on the slant surface depends on the specific flow regime and control conditions. Therefore, focusing on the SPOD mode associated with the actuation, it is possible to study the extension of the region where the flow is receptive to the action of control (locking region).

Figure 15 shows the pressure fluctuation signature on the ramp associated with the actuation frequencies of the first SPOD pressure modes at different Re_H numbers. Overall the extension of the region influenced by the action of pulsed jets is reduced with increasing the actuation frequency at a given Reynolds number. At the lowest velocity regime ($Re_H = 1.4 \times 10^5$) and minimum control frequency [Fig. 15(a)], the low-pressure zone is followed by a pressure recovery and spanwise variations on the ramp, meaning that the influence of the jets extends well downstream into the flow field. For higher frequency values, the intensity of the pressure recovery is stronger [Fig. 15(b)] and the pressure recovery region moves towards the sharp edge, with a restricted peak area located around the midplane [Fig. 15(c)]; a further increase in frequency produces a pressure uniform distribution on the downstream part of the ramp [Fig. 15(d)], confining the influence region of the pulsed jets close to the sharp edge. When Re_H increases [Figs. 15(e)–15(h) for $Re_H = 2.1 \times 10^5$] the pressure signals exhibit strong streamwise variations for all actuation frequencies a more uniform distribution in the spanwise direction [Figs. 15(i)–15(l) for $Re_H = 2.8 \times 10^5$]. Note that at $Re_H = 2.1 \times 10^5$ (second line of Fig. 15) the figures refer to a duty cycle equal to DC = 50%. Therefore one can conclude that the action of the control produces an oscillating pressure pattern along the streamwise direction, while the regions not influenced by the actuation are characterized by a uniform pressure.

Note that since all pressure probes are located on one side of the ramp, the pressure SPOD modes could in principle exhibit a symmetric or an antisymmetric behavior. However, physical considerations made *a posteriori* on the obtained results allowed us to conclude that the modes are symmetrical. In particular, the PIV measurements confirm that the lowest frequency mode, in both the uncontrolled and controlled configurations, is linked to the occurrence of two vortices that exhibit an in-phase motion in the transverse plane (and therefore they are supposed to be symmetric). Regarding the SPOD modes associated with the flapping motion and the large-scale vortex emission from the shear layer at the slant edge, they are expected to be symmetric because of the nature of the recirculating bubble. By the same reasoning, the modes related to the onset of Kelvin-Helmholtz instability and the ones related to the action of the pulsed actuators, acting in-phase on the whole slant, are expected to be symmetric as well.

B. Hot-wire measurements

The analysis of the SPOD spectra has highlighted relevant frequencies of the flow and the underlying coherent structures associated with the spatial distributions of the SPOD modes. Hot-wire velocity measurements are analyzed here to obtain further insight into the characteristic timescales of the flow.

In particular measurements of probes A, B, G, and I of Fig. 4, which are located in the two longitudinal planes $y/H = 0$ and $y/H = 1.9$, have been analyzed. In the midplane and uncontrolled conditions, probes A and B lie in the shear layer near the slant edge, probe G is located in the recirculation bubble, close to the wall and slightly upstream of the reattachment point, whereas probe I is immediately past the reattachment point. In the plane $y/H = 1.9$ all probes are located within the side roll-up structure.

The normalized crosswise velocity power spectral density (PSD) at $Re_H = 1.4 \times 10^5$ in absence of control is shown in Fig. 16 as a function of the Strouhal number. In the midplane (blue curves) the spectra of probes A [Fig. 16(a)] and B [Fig. 16(b)] exhibit two peaks: (1) a lower peak occurring, in agreement with the findings of the SPOD analysis, at $St \approx 0.04$ for both probes (and related to the flapping motion of the recirculation region) and (2) a higher peak associated with the

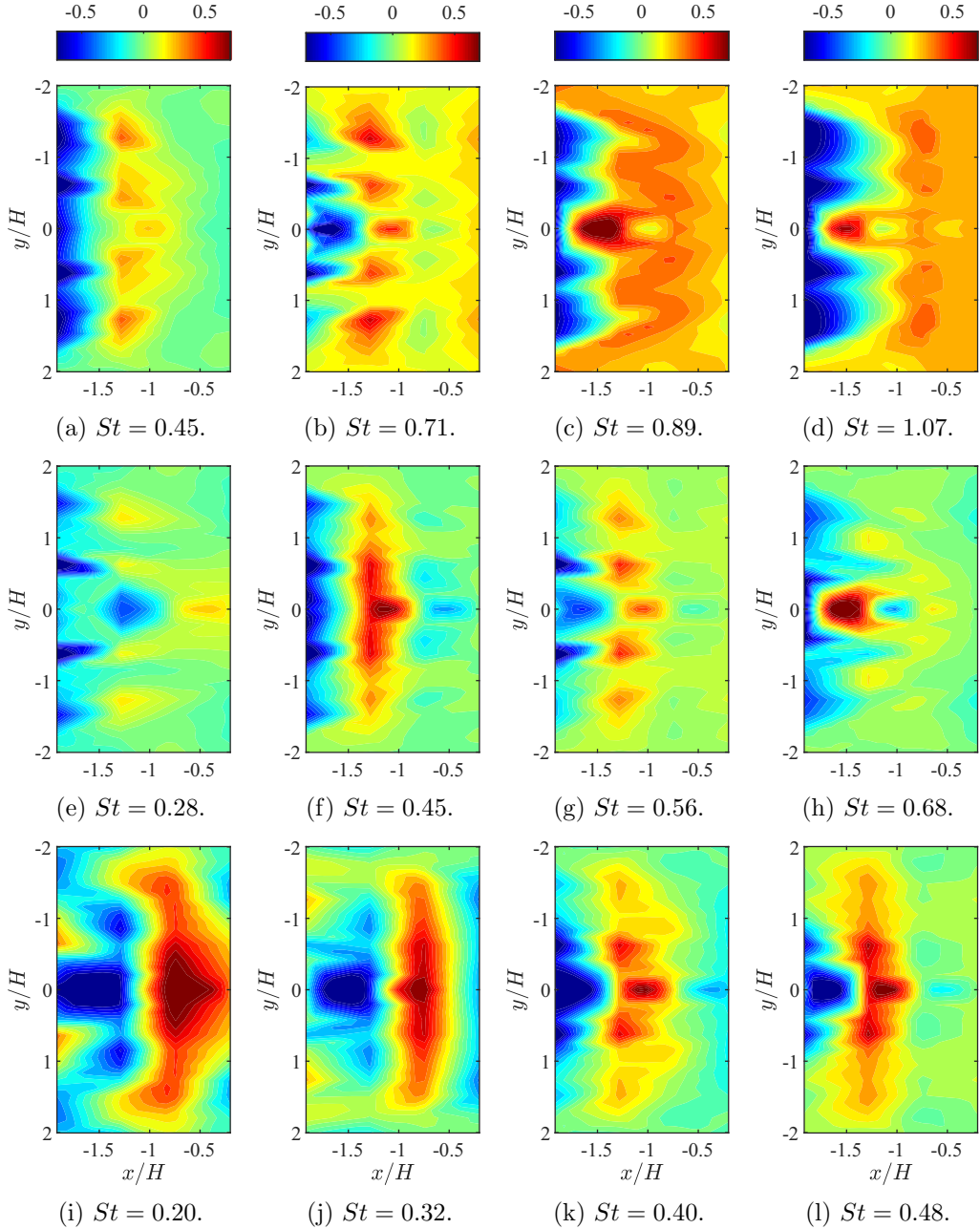


FIG. 15. Spatial structures associated with the actuation frequencies of the first SPOD pressure modes at $Re_H = 1.4$ (first line), $Re_H = 2.1$ (second line), and 2.8×10^5 (third line). The surface contours represent the normalized pressure fluctuation signature on the ramp.

Kelvin-Helmholtz instability in the thin shear layer. In agreement with results from linear stability analysis of two-dimensional free shear layers [18,28], the frequency of the second peak depends on the probe location and diminishes when moving downstream. Probes G and I, located very close to the flat plate, are most sensitive to the impact of the shedding vortices on the wall, and the St peak

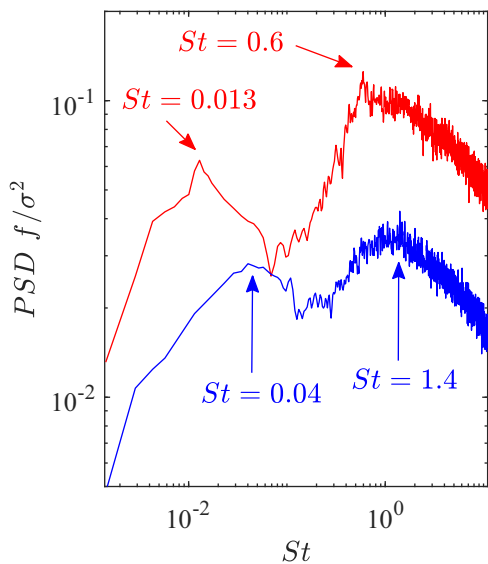
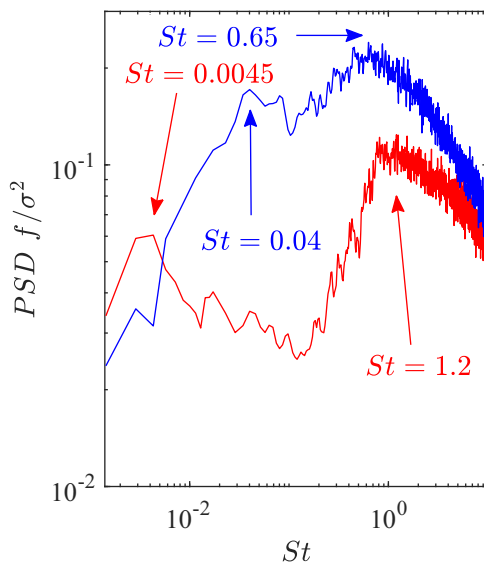
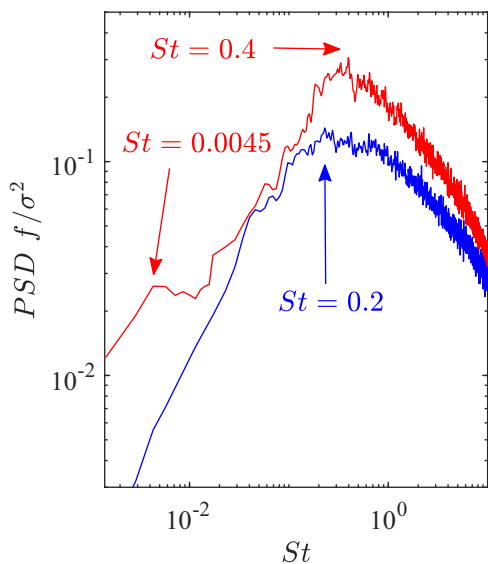
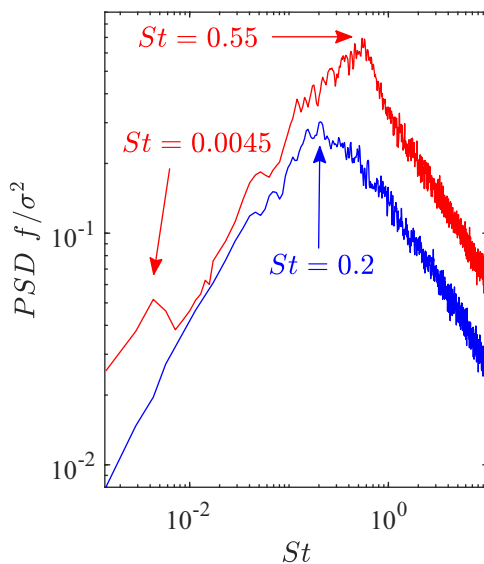

 (a) A probe ($x/H = -1.81$, $z/H = 1.01$).

 (b) B probe ($x/H = -1.28$, $z/H = 0.96$).

 (c) G probe ($x/H = 0.53$, $z/H = 0.11$).

 (d) I probe ($x/H = 1.12$, $z/H = 0.37$).

 FIG. 16. Normalized velocity power spectral density as a function of the Strouhal number for different locations in planes $y/H = 0$ (blue curves) and $y/H = 1.9$ (red curves). $Re_H = 1.4 \times 10^5$.

is approximately 0.2 (in good relation with the edge tones). In the plane $y/H = 1.9$, the probes do not lie in the recirculation bubble, and they are affected by the two streamwise roll-up vortices that develop from the slant side edges, inducing a downwash on the slant surface. The relative spectra do not exhibit the characteristic frequencies of neither flapping nor vortex shedding modes. On the contrary, peaks related to the oscillations of the longitudinal vortex structures, at the frequencies of $St \approx 0.013$ and $St \approx 0.0045$, are clearly visible for all probes (red curves of Fig. 16).

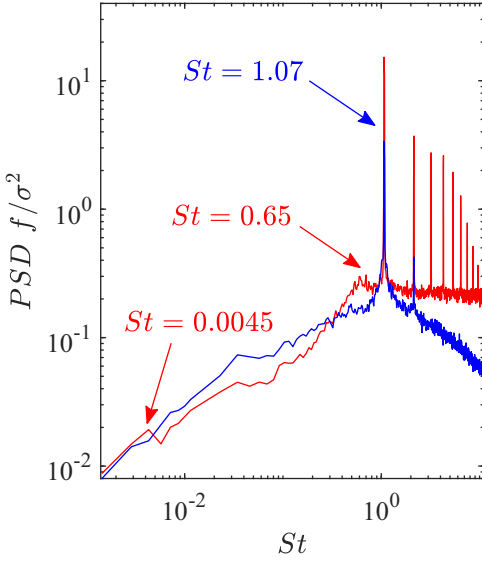
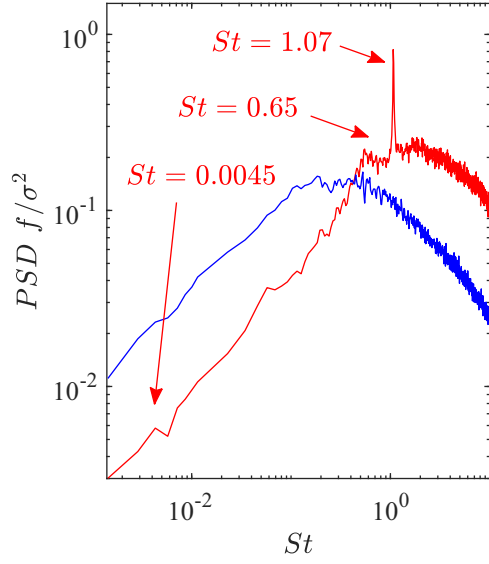
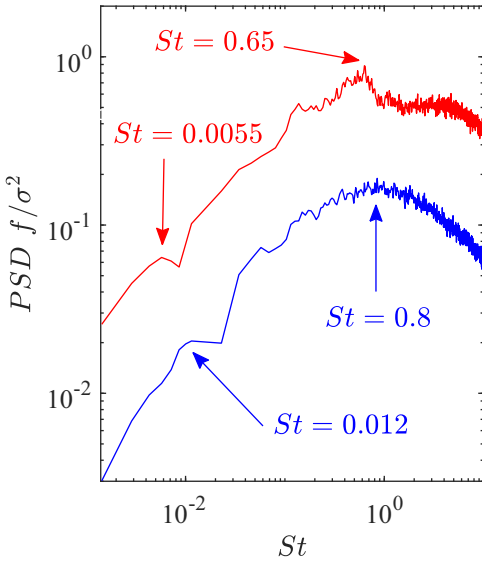
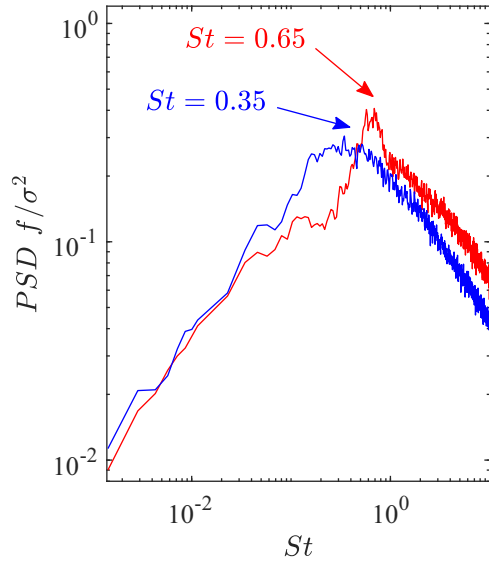

 (a) A probe ($x/H = -1.81$, $z/H = 1.01$).

 (b) B probe ($x/H = -1.28$, $z/H = 0.96$).

 (c) G probe ($x/H = 0.53$, $z/H = 0.11$).

 (d) I probe ($x/H = 1.12$, $z/H = 0.37$).

 FIG. 17. Normalized velocity power spectral density as a function of the Strouhal number for different locations in planes $y/H = 0$ (blue curves) and $y/H = 1.9$ (red curves). $Re_H = 1.4 \times 10^5$ and $St_a = 1.07$.

Considering now the flow in controlled conditions, the spectrum is dominated by the actuation frequency and its higher harmonics, depending on the specific Re_H and control parameters. Figure 17 shows the PSD of the crosswise velocity data (taking into account the measurements acquired with the same probes as above) at $Re_H = 1.4 \times 10^5$ and $St_a = 1.07$. In this case the control authority of the pulsed jets is limited to the probes close to the sharp edge, as highlighted before, and differs in the various locations. Indeed, probe A [Fig. 17(a)], which is the closest one to the sharp

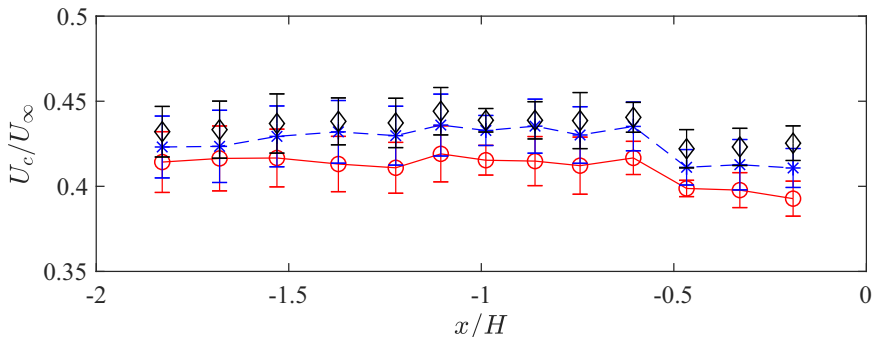


FIG. 18. Average convection velocity of shedding vortices as a function of the streamwise direction. Red line $Re_H = 1.4 \times 10^5$, blue lines $Re_H = 2.1 \times 10^5$, black lines $Re_H = 2.8 \times 10^5$.

edge, shows a spectrum at $y/H = 0$ (red curve) peaked at $St \approx 1.07$, with just one higher harmonic, and a rapid decay at high frequencies; the same probe at $y/H = 1.9$ (blue curve) presents a spectrum largely dominated by the control frequency and its harmonics, with a slow decay with frequency, but also a light peak at $St \approx 0.0045$, due to the longitudinal vortex structures, and another one at $St \approx 0.65$ associated with the Kelvin-Helmholtz instability in the thin shear layer developing at the slant sides only. These spectral differences agree very well with the SPOD results; indeed, the SPOD pressure pattern associated with the control [Fig. 15(d)] shows a recovery region in the midplane while the slant edges present a low-pressure distribution, typical of a higher penetration of the jet influence. Moving downstream, the effect of the pulsed jets decreases, and the spectrum does not exhibit the control frequency in the midplane, which is still evident at the $y/H = 1.9$ together with a peaks at $St \approx 0.0045$ and $St \approx 0.65$. After the hinge line, the spectrum is not affected anymore by the pulsed jets in any location. In the middle plane, probe G [Fig. 15(c)] presents a local peak at $St \approx 0.012$, associated with a streamwise vortex structure, and a maximum around $St \approx 0.8$ (a typical frequency ascribed to the Kelvin-Helmholtz instability that could arise at the sharp edge), which is reduced at $St \approx 0.35$ for the probe I [Fig. 15(c)]. At the slant edges, instead, the probe shows a local peak at $St \approx 0.0055$ and a maximum at $St \approx 0.65$, which is retrieved also in the probe I spectrum.

C. Further physical considerations

As discussed in Sec. III B, the streamwise convection velocity in uncontrolled conditions of the traveling structures has been determined directly from the analysis of cross-correlation of pressure data. Figure 18 shows the normalized convection velocity (U_c/U_∞) as a function of the streamwise location for the three Reynolds numbers. The figure shows that U_c/U_∞ varies between 0.39 and 0.44 depending on the longitudinal position, with slightly higher values at higher Reynolds numbers.

We have previously argued that in the range $0.055 < St < 0.45$, the shedding of large-scale vortices emitted from the slant edge, propagating along the shear layer and impacting on the slant, shares similarities with the edge tone phenomenon. We recall that the latter is associated with the formation of primary and secondary vortices produced by a jet issuing from a nozzle that impact on a wedge (called edge) placed in the stream. Under certain circumstances, this results in the generation of (sound) tones in the unstable frequency band of the jet [27]. The frequencies of such tones depend on a variety of physical parameters, such as the width of the jet, the distance between the source of the perturbation and the impact point, the wavelength of the oscillation, the convection velocity, and the different shapes (called the stages of the edge tone) that the oscillating jet can take [29]. In

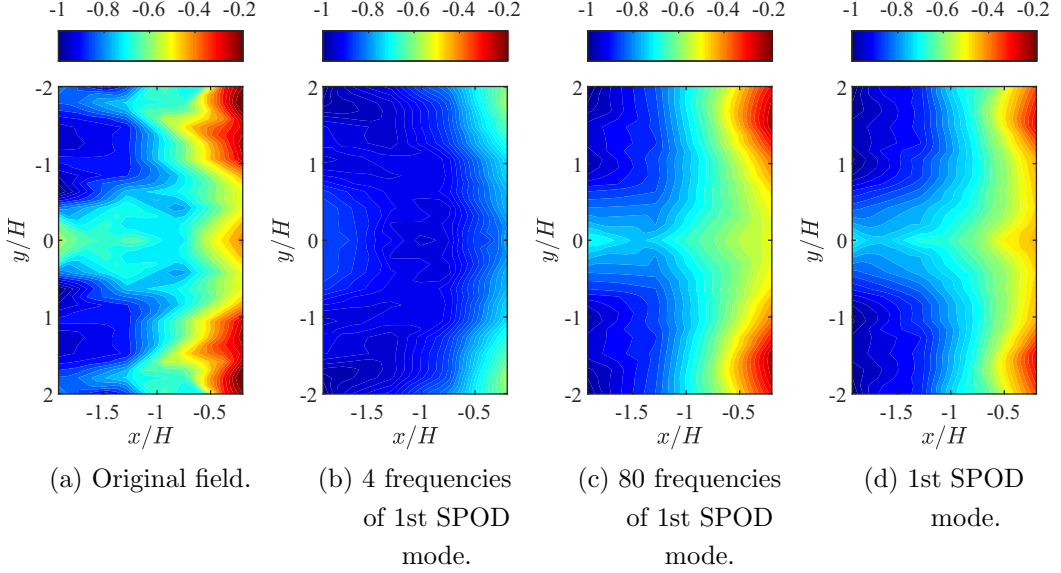


FIG. 19. Comparison of the original pressure snapshot (a) and the reconstructed field with four, 80, and all [(b) to (d), respectively] frequencies of the first SPOD mode. $Re_H = 1.4 \times 10^5$. The flow direction is from left to right. The normalized pressure fluctuation is shown.

particular, Curle [27], Vaik *et al.* [29], and other authors give the following relations:

$$d_{et} = (n + \varepsilon)\lambda_{et}, \quad (5)$$

$$f = \frac{U_c}{\lambda_{et}} \quad \text{or equivalently} \quad St = \frac{fH}{U_\infty} = (n + \varepsilon) \frac{U_c}{U_\infty} \frac{H}{d_{et}}, \quad (6)$$

where d_{et} and f are, respectively, the distance between the vortex source and the edge and the frequency. Furthermore, λ_{et} is the distance between two consecutive vortices, n is an integer standing for the stage of the edge tone and corresponds to the number of wavelengths between the vortex source and the edge, and ε is a small number (different values of ε are found in the literature; for example, Ref. [27] gives $\varepsilon = 0.25$, while other authors indicate a value of 0.5 [29]).

If one takes for λ_{et} the streamwise distance between two consecutive pressure minima [two consecutive blue valleys from Fig. 8(c)] one finds $\lambda_{et}/H \approx 2$, and if one assumes that the distance between the slant edge and the impact point coincides with the reattachment length, one obtains $d_{et}/H \approx 3$. Hence, one can argue that the scale factor is $3/2$, which corresponds to $\varepsilon \approx 0.5$, for a first stage edge tone ($n = 1$). Using the average normalized convective velocity of $U_c \approx 0.4$, from Eq. (6) one obtains a Strouhal number of $St \approx 0.2$ in agreement with the results from SPOD-modes results, thus corroborating our argument that the shedding of large-scale vortices impacting on the slant shares similarities with the edge tone phenomenon.

D. Pressure field reconstruction

From the spectral decomposition the instantaneous pressure field can be reconstructed applying the inverse Fourier transform to the blocks computed with Eq. (2). The reconstruction can be carried out either considering a reduced number of SPOD modes, or applying a high-pass filter, namely, by taking into account only a few relevant frequencies of the first SPOD mode.

Figure 19 shows the comparison between the original pressure field at a given time instant [Fig. 19(a)] and the corresponding field reconstructed accounting both for a reduced number of

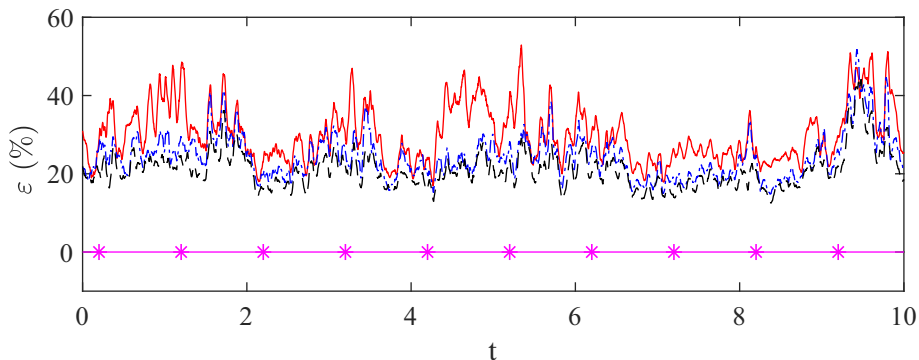


FIG. 20. Evolution of the reconstruction error, $\varepsilon(t)$, with time for reconstructed fields based on: four (red continuous line), 80 (blue dash-dotted line), and all (black dashed line) frequencies of the first SPOD mode. The magenta line refers to the reconstruction with all SPOD modes. $\text{Re}_H = 1.4 \times 10^5$.

frequencies of the first SPOD mode only [Figs. 19(b) and 19(c)] and for the (entire) first SPOD mode [Fig. 19(d)], for the reference case $\text{Re}_H = 1.4 \times 10^5$. In particular, Fig. 19(b) contains the reconstruction based on four frequencies, one for each of the four characteristic bands of the spectrum associated with the local peak frequencies. This choice is related to the particular trend of the spectrum that features separation intervals exhibiting a nearly flat shape with no distinct peaks. With this limited number of frequencies the cumulative energy ratio is $\text{ER} = \sum_{\tilde{k}} \lambda_{1\tilde{k}} / \sum_{j,k} \lambda_{jk} = 0.8\%$, where \tilde{k} is a running index of selected frequencies, and the field is not adequately reconstructed. Increasing the number of frequencies up to 80 (20 frequencies for each band of the spectrum, centered around the maximum separation between the first and the second mode), the cumulative energy ratio is equal to $\text{ER} = 28.5\%$, obtaining a better pressure field reconstruction [Fig. 19(c)]. Finally, Fig. 19(d) shows the field reconstructed by considering all frequencies of the first SPOD mode; in this case, the reconstruction keeps getting better ($\text{ER} = 50.9\%$), the field appearing smoothed out compared to the original snapshot.

Let ε be the reconstruction error defined as

$$\varepsilon(t) = \frac{\|\mathbf{q}(\mathbf{x}, t) - \tilde{\mathbf{q}}(\mathbf{x}, t)\|}{\|\mathbf{q}(\mathbf{x}, t)\|}, \quad (7)$$

where $\|\cdot\|$ represents the L_2 norm, $\mathbf{q}(\mathbf{x}, t)$ is a snapshot at a given time, and $\tilde{\mathbf{q}}(\mathbf{x}, t)$ represents its reconstruction. The evolution of the reconstruction error, $\varepsilon(t)$, with time is shown in Fig. 20. The reconstruction based on four frequencies (red continuous line) shows strong variations with time, with a mean value around 31.2%. Increasing the number of modes, the reconstruction error decreases down to 24.6% for 80 frequencies (blue dash-dotted line) and to 21.2% for all frequencies (black dashed line) of the first SPOD mode. As expected, with all SPOD modes a null reconstruction error is retrieved (magenta line).

The same reconstruction approach has been applied also for the controlled conditions. In particular, Fig. 21 compares the original pressure field at a given time instant [Fig. 21(a)] to the corresponding reconstructed fields with four, 80, and all [Figs. 21(b)–21(d), respectively] frequencies of the first SPOD mode, at $\text{Re}_H = 1.4 \times 10^5$ and $\text{St}_a = 1.07$. Here the reconstruction based on the least number of frequencies has a cumulative energy ratio $\text{ER} = 36.7\%$, reproducing the main characteristics of the original field. This is related to fact that control affects the spectrum producing a uniform distribution of power per mode, with narrow peak intervals, and as a result a restricted number of specific frequencies contains most of the energy. ER increases to 50.8% and 76.9% when considering 80 and all frequencies of the first SPOD mode, respectively.

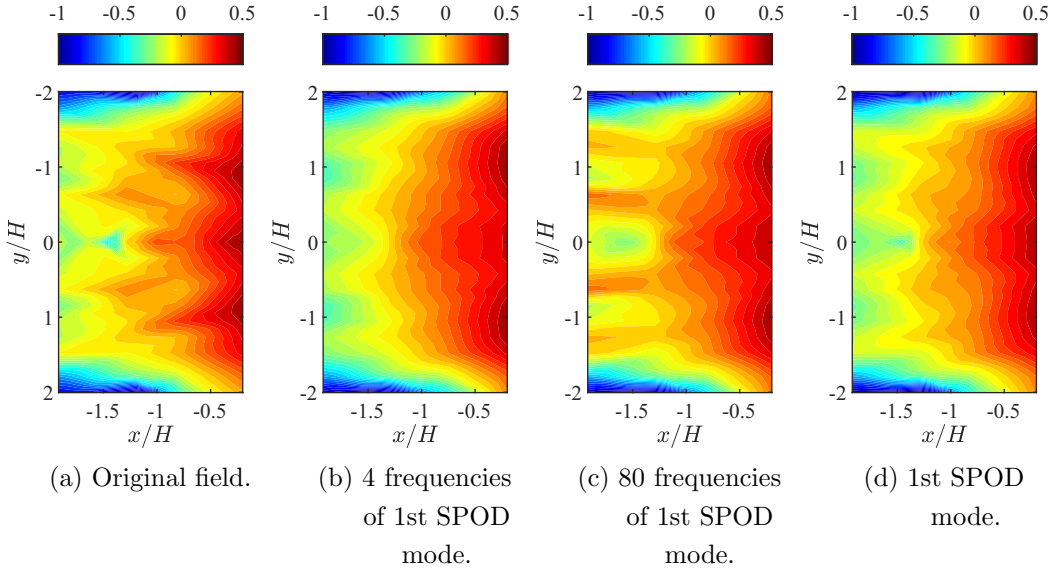


FIG. 21. Comparison of the original pressure snapshot (a) and the reconstructed field with four, 80, and all [(b) to (d), respectively] frequencies of the first SPOD mode in the case of controlled conditions. $Re_H = 1.4 \times 10^5$ and $St_a = 1.07$. The flow direction is from left to right. The normalized pressure fluctuation is shown.

It is important to point out that the increase in the cumulative energy ratio does not imply a reduction of the average reconstruction error, which depends also on the mode separation. Indeed, as shown in Fig. 22, the reconstruction based on four frequencies presents an average error of about 37.6%, which is higher than the corresponding one for the uncontrolled conditions. Moreover, for this case, it is interesting to observe a periodic behavior with a time interval of 1 s, which corresponds to the temporal width of the SPOD blocks. Reconstructions based on a higher number of frequencies show a uniform error variation with mean values of 24.6% and 21.2% for 80 and all frequencies of the first SPOD mode, respectively.

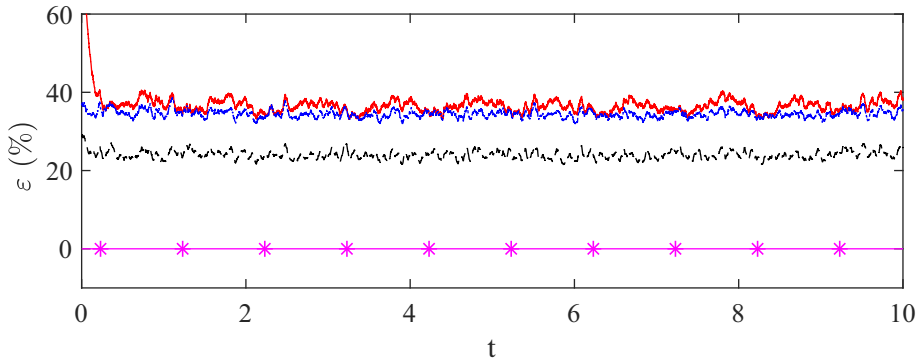


FIG. 22. Evolution of the reconstruction error, $\varepsilon(t)$, with time for reconstructed fields based on: four (red continuous line), 80 (blue dash-dotted line), and all (black dashed line) frequencies of the first SPOD mode. The magenta line refers to the reconstruction with all SPOD modes. $Re_H = 1.4 \times 10^5$ and $St_a = 1.07$.

V. CONCLUSIONS

The dynamics of the separated flow behind a finite span backward-facing ramp in controlled and uncontrolled conditions has been investigated applying spectral proper orthogonal decomposition (SPOD) to unsteady pressure and stereo-PIV measurements. The control is performed with 89 pulsed jets (normal to the mean flow direction) operating at various frequency (St_d) and duty cycle (DC) values.

Three different Reynolds numbers ($Re_H = 1.4, 2.1, 2.8 \times 10^5$), with several actuation frequency and duty cycle values, have been considered, for a total of 12 different flow conditions. The role of the most energetic and dynamically relevant coherent structures has been identified in both regimes.

Considering first the uncontrolled case, the SPOD analysis recognized four frequency bands that show a clear spectral mode separation, implying a low-rank behavior of the flow. These frequencies are associated with the presence of two large-scale longitudinal roll-up vortices which oscillate at the slanted ramp side edges; the flapping motion of the recirculation bubble; the large-scale vortex emission from the shear layer at the slant edge, which is reminiscent of the acoustic self-resonance phenomenon usually referred to as edge tones; and the onset of Kelvin-Helmholtz instability in the separated shear layer just downstream of the sharp edge.

The convective velocity of the shedding vortex structures and their wavelength have been evaluated via SPOD, and the shedding mode has been interpreted as an edge-tone phenomenon by means of distinguishing relationships.

The control suppresses the recirculation due to separation, and its action is the removal of the flapping mode and of the large-scale vortex emission from the shear layer at the slant edge, hence the spectrum does not exhibit the peak frequencies typical of these mechanisms. As expected, the mode related to the lateral roll-up vortices persists. Two other modes, a nonsymmetric structure around the middle plane, and smaller structures localized at the slant edges only, have been detected, which are attributed to the operation of the present actuation system. Finally, the spectrum is dominated by several other peaks occurring at the actuation frequency and its harmonics.

The control authority of the pulsed jets has been evaluated in detail considering the pressure fluctuation signature on the ramp associated with the actuation frequencies of the first SPOD pressure modes at different Re_H numbers. The action of the control produces an oscillating pressure pattern along the streamwise direction of the slant surface, while the regions not influenced by the actuation are characterized by a uniform pressure values. In general, the extension of the locking region is reduced with increasing the actuation frequency for a given Reynolds number; when Re_H increases, the locking region extends on the whole slant surface for all considered frequencies. From a practical viewpoint focusing on the SPOD mode associated with the actuation allows one to study the extension of the region where the flow is receptive to the action of control.

Overall the SPOD modes exhibit a peculiar behavior featuring multiple mechanisms in the different controlling frequency bands and suggesting the use of specific SPOD modes for low-order reconstruction. In particular, one SPOD mode reproduces the dynamics of the pressure field with a reconstruction error lower than the 25% for both the uncontrolled and controlled cases.

ACKNOWLEDGMENTS

The authors acknowledge the staff of Institut Aerotechnique for the experimental database developed in the framework of projects CARS, CAJE and CABOF funded by Institut Carnot ARTS. The authors also wish to thank Antonio Colanera for his support in the implementation of the SPOD reconstruction technique.

[1] C. W. Rowley and S. T. M. Dawson, Model reduction for flow analysis and control, *Annu. Rev. Fluid Mech.* **49**, 387 (2017).

- [2] K. Taira, S. L. Brunton, S. T. M. Dawson, C. W. Rowley, T. Colonius, B. J. McKeon, O. T. Schmidt, S. Gordyev, V. Theofilis, and L. S. Ukeiley, Modal analysis of fluid flows: An overview, *AIAA J.* **55**, 4013 (2017).
- [3] A. Towne, O. T. Schmidt, and T. Colonius, Spectral proper orthogonal decomposition and its relationship to dynamic mode decomposition and resolvent analysis, *J. Fluid Mech.* **847**, 821 (2018).
- [4] C. Cuvier, J. M. Foucaut, C. Braud, and M. Stanislas, Characterisation of a high Reynolds number boundary layer subject to pressure gradient and separation, *J. Turbulence* **15**, 473 (2014).
- [5] P. Gilliéron, A. Leroy, S. Aubrun, and P. Audier, Influence of the slant angle of 3D bluff bodies on longitudinal vortex formation, *J. Fluids Eng.* **132**, 051104 (2010).
- [6] A. Sciacchitano and D. Giaquinta, Investigation of the Ahmed body cross-wind flow topology by robotic volumetric PIV, in *Proceedings of the 13th International Symposium on Particle Image Velocimetry: 22–27 July, Munich, Germany*, edited by C. J. Kähler, R. Hain, S. Scharnowski, and T. Fuchs (Universität der Bundeswehr München, 2019), pp. 311–320.
- [7] A. Thacker, S. Aubrun, A. Leroy, and P. Devinant, Experimental characterization of flow unsteadiness in the centerline plane of an Ahmed body rear slant, *Exp. Fluids* **54**, 1479 (2013).
- [8] S. Ahmed, G. Ramm, and G. Faltin, Some salient features of the time-averaged ground vehicle wake, in *Proceedings of SAE International Congress and Exposition, Detroit, Michigan* (SAE International, 1984).
- [9] S. Krajnovic and L. Davidson, Flow around a simplified car, part 1: Large eddy simulation, *J. Fluids Eng.* **127**, 907 (2005).
- [10] S. Krajnovic and L. Davidson, Flow around a simplified car, part 2: Understanding the flow, *J. Fluids Eng.* **127**, 919 (2005).
- [11] A. Brunn and W. Nitsche, Active control of turbulent separated flows over slanted surfaces, *Int. J. Heat Fluid Flow* **27**, 748 (2006).
- [12] J. Dandois, E. Garnier, and P. Sagaut, Numerical simulation of active separation control by a synthetic jet, *J. Fluid Mech.* **574**, 25 (2007).
- [13] P.-Y. Pamart, J. Dandois, E. Garnier, and P. Sagaut, Large eddy simulation study of synthetic jet frequency and amplitude effects on a rounded step separated flow, in *5th Flow Control Conference, Chicago, Illinois* (AIAA, Reston, VA, 2010), pp. 1–11.
- [14] V. Kumar and F. S. Alvi, Toward understanding and optimizing separation control using microjets, *AIAA J.* **47**, 2544 (2009).
- [15] A. Debien, S. Aubrun, N. Mazellier, and A. Kourta, Active separation control process over a sharp edge ramp, in *9th International Symposium on Turbulence and Shear Flow Phenomena* (TSFP Digital Library Online, 2015), pp. 341–346.
- [16] A. Kourta, A. Thacker, and R. Jossot, Analysis and characterization of ramp flow separation, *Exp. Fluids* **56**, 104 (2015).
- [17] A. Debien, K. A. F. F. von Krbek, N. Mazellier, T. Duriez, L. Cordier, B. R. Noack, M. W. Abel, and A. Kourta, Closed-loop separation control over a sharp edge ramp using genetic programming, *Exp. Fluids* **57**, 40 (2016).
- [18] D. Hlevca, P. Gillieron, and F. Grasso, Experimental study of the active control applied to the flow past a backward facing ramp, *Exp. Fluids* **59**, 39 (2018).
- [19] M. Chiatto, D. Hlevca, L. de Luca, and F. Grasso, Modal analysis of actively controlled flow past a backward facing ramp, in *Proceedings of AIAA SciTech Forum, AIAA paper 2020-0100, 6–10 January, Orlando, Florida* (AIAA, Reston, VA, 2020), pp. 1–13.
- [20] O. T. Schmidt and T. Colonius, Guide to spectral proper orthogonal decomposition, *AIAA J.* **58**, 1023 (2020).
- [21] A. Nekkanti and O. T. Schmidt, Frequency-time analysis, low-rank reconstruction and denoising of turbulent flows using SPOD, [arXiv:2011.03644](https://arxiv.org/abs/2011.03644).
- [22] J. F. Largeau and V. Moriniere, Wall pressure fluctuations and topology in separated flows over a forward facing step, *Exp. Fluids* **42**, 21 (2007).
- [23] C. P. Van Dam, Recent experience with different methods of drag prediction, *Prog. Aerospace Sci.* **35**, 751 (1999).
- [24] M. Kiya and K. Sasaki, Structure of a turbulent separation bubble, *J. Fluid Mech.* **137**, 83 (1983).

- [25] B. Armaly, F. Durst, J. C. F. Pereira, and B. Schönung, Experimental and theoretical investigation of backward-facing step flow, *J. Fluid Mech.* **127**, 473 (1983).
- [26] N. J. Cherry, R. Hillier, and M. E. Latour, Unsteady measurements in a separated and reattaching flow, *J. Fluid Mech.* **144**, 13 (1984).
- [27] N. Curle, The mechanics of edge-tones, *Proc. R. Soc. London A* **216**, 412 (1953).
- [28] P. Huerre and M. Rossi, Hydrodynamic instabilities in open flows, in *Hydrodynamics and Nonlinear Instabilities*, edited by C. Godrèche and P. Manneville (Cambridge University Press, Cambridge, 1998), pp. 81–294.
- [29] I. Vaik, R. Varga, and G. Paál, Frequency and phase characteristics of the edge tone: Part II, *Period. Polytech., Mech. Eng.* **58**, 69 (2014).